Journal of Geoscience and Environment Protection, 2026, 14(1), 19-42
https://www.scirp.org/journal/gep
ISSN Online: 2327-4344
ISSN Print: 2327-4336

Characterization of Microscale Heterogeneities in the Sedimentary Deposits of the Morro Pelado Member, Rio do Rasto Formation, Paraná Basin: Implications for Reservoir Quality

Alexandra Nicole Sanchez Hidalgo[1], Manoela Bettarel Bállico[1], Celso Peres Fernades[1], Monica Oliveira Manna[1], Rodrigo Nagata[2], Anderson Camargo Moreira[2], Iara Frangiotti Mantovani[2], Maiara Silva Baltazar[3], Ezequiel Galvão de Souza[4]

[1]Department of Geosciences, Graduate Program in Geology, Reservoir Geology Laboratory, Federal University of Santa Catarina, Florianopolis, Brazil
[2]Laboratory of Porous Media and Thermophysical Properties (LMPT), PGMAT/EMC, Federal University of Santa Catarina, Florianopolis, Brazil
[3]Department of Geosciences, Reservoir Geology Laboratory, Federal University of Santa Catarina, Florianopolis, Brazil
[4]Universidade Federal do Pampa, Caçapava do Sul, Brazil
Email: alenicosh1997@gmail.com

How to cite this paper: Hidalgo, A. N. S., Bállico, M. B., Fernades, C. P., Manna, M. O., Nagata, R., Moreira, A. C., Mantovani, I. F., Baltazar, M. S., & de Souza, E. G. (2026). Characterization of Microscale Heterogeneities in the Sedimentary Deposits of the Morro Pelado Member, Rio do Rasto Formation, Paraná Basin: Implications for Reservoir Quality. *Journal of Geoscience and Environment Protection, 14,* 19-42.
https://doi.org/10.4236/gep.2026.141002

Received: November 22, 2025
Accepted: January 12, 2026
Published: January 15, 2026

Abstract

This article presents the petrophysical and depositional characterization of the Morro Pelado Member of the Rio do Rasto Formation. Sandstones from eolian and fluvial depositional system were analyzed to understand the variability of the pore system. For this purpose, petrographic analyses, mercury intrusion porosimetry (MIP), and X-ray computed microtomography (Micro-CT) were integrated, enabling a multiscale assessment of the petrophysical characteristics. The results revealed highly heterogeneous pore systems, with total porosity ranging between 0.33% and 25.53% and permeability values oscillating from less than 3 mD to over 2400 mD. The best reservoirs were identified in fluvial sandstones, particularly in the facies of lateral accretion bars and aggradational sandy bedforms, associated with high primary porosity, good pore connectivity, and low carbonate cement content. In contrast, the eolian sandstones behave as unconventional reservoirs, with systems dominated by micropores, narrow pore throats, and low connectivity. In the overbank deposits, high-productivity reservoirs were observed in terminal splays, contrasting with matrix- and carbonate cement-rich units. Permeability anisotropy and the presence of dual porosity stood out as essential factors in controlling subsurface flow. The integrated analyses reinforce the need for applying multiscale models

in the petrophysical characterization of the unit, considering the contribution of isolated microporosity and the role of sedimentary structures in orienting preferential flow paths. The obtained results highlight the potential of the Morro Pelado Member as a heterogeneous siliciclastic reservoir, with relevance for hydrogeological studies.

Keywords

Morro Pelado Member, Pore System, Reservoir

1. Introduction

Access to water is a fundamental pillar of collective well-being, making its sustainable supply a global priority. In this context, aquifers stand out as a crucial source of water. According to Hirata et al. (2019), groundwater constitutes the largest reservoir of potable water on the planet, representing approximately 97% of all fresh liquid water. This resource is vital for water security, being essential not only for human supply and various economic activities but also for maintaining ecosystems such as rivers, lakes, and forests in dry climate regions, which depend on these underground sources to preserve their environmental functions.

In southern Brazil, siliciclastic formations demonstrate significant potential for water resource exploitation. While the Botucatu Formation, part of the Integrated Guarani/Serra Geral Aquifer System (SAIG/SG) is established as one of the largest global aquifers (Filho et al., 2023), the Rio do Rasto Formation emerges as a strategic geological unit in the region. Its composition is marked by high faciological heterogeneity, an attribute that, while presenting challenges for hydrogeological modeling, confers uniqueness to its pore system, as evidenced by studies reporting porosities between 4.2% (Fernandes, 2009) and 12.58% (Dal Col et al., 2016), with critical variations in pore size and distribution (2.9 - 30 μm). Such discrepancies reinforce the need for integrated analyses, combining micro-CT with conventional methods, for a reliable assessment of water potential.

Permeability and porosity are fundamental parameters in the characterization of reservoir rocks, as they determine the storage capacity and fluid flow within the reservoir rock (Tiab & Donaldson, 2024). Traditional methods, such as mercury intrusion porosimetry and Darcy's law-based tests, provide direct measurements of these properties. However, advanced techniques, like X-ray computed microtomography (micro-CT), enable the acquisition of microtomographic sections and the three-dimensional reconstruction of the internal structure of samples, providing qualitative and quantitative data on the morphology, size, distribution, volume, surface area, and connectivity of pores at a micrometer scale (Neto et al., 2011).

The Rio do Rasto Formation outcrops significantly in the state of Santa Catarina, where its aquifer potential holds great relevance for supplying urban centers, such as the city of Lages. To ensure the effectiveness and preservation of this in-

dispensable resource, adequate characterization of the rocks that compose these reservoirs becomes imperative.

2. Geological Context

The Paraná Basin, one of the main magmatic-sedimentary provinces in South America, developed between the Neordovician and the Neocretaceous, spanning a Paleozoic-Mesozoic interval (Milani et al., 2007). With an approximate area of 1,700,000 km^2, this basin covers the southern portion of Brazil, eastern Paraguay, northeastern Argentina, and northern Uruguay (Holz et al., 2010; Scherer et al., 2023). The Paraná Basin has an elongated north-south geometry and its stratigraphic framework can reach thicknesses of up to 7.5 km at its depocentre (Milani et al., 2007). The Paraná Basin's geographic boundaries are erosive and associated with tectonic events affecting the South American Platform, particularly during the Meso-Cenozoic era, when the South Atlantic Ocean opened up (Milani et al., 2007). The main lineaments display NW-SE and NE-SW orientations, which are associated with the reactivation of basement structures, as well as E-W lineaments, which are related to lithospheric stresses resulting from the opening of the South Atlantic (Zalán et al., 1990).

Rio do Rasto Formation

The Rio do Rasto Formation is a notable sedimentary record in the Paraná Basin associated with western Gondwana continentalization among the Middle to Upper Permian (Milani et al., 2007; Holz et al., 2010; Scherer et al., 2023). This unit reaches thicknesses up to 600 meters and outcrops along the eastern margin of the Paraná Basin in South Brazil. The Rio do Rasto Formation is divided in two lithostratigraphic units: the basal Serrinha Member, and the upper Morro Pelado Member (Gordon Jr., 1947).

The Serrinha Member consists of greenish-gray and purple claystones and siltstones interbedded with fine-grained gray sandstone (Schneider et al., 1974; Holz et al., 2010; Scherer et al., 2023). This unit may reach thicknesses between 150 and 250 meters, and the transition to the Morro Pelado Member is concordant and gradual, primarily characterized by an increase in sandy deposits upward.

The Morro Pelado Member corresponds to the thickest interval and may reach thicknesses of 250 to 300 meters (Schneider et al., 1974; Holz et al., 2010). This unit is characterized by an increased occurrence of sandy bodies interbedded with claystones and siltstones throughout the succession. These fine-grained rocks become more reddish toward the top, indicating more oxidizing conditions than those in the basal portion (Lavina, 1991; Scherer et al., 2023). Additionally, paleosols and pedogenetic features become more prevalent towards the top of the Morro Pelado Member.

Due to the common intercalation of sandstone and fine-grained rocks with a variety of sedimentary structures, the Rio do Rasto Formation is interpreted as having been deposited by many paleoenvironments. These environments include

transitional tidal flats (Schneider et al., 1974); a wide deltaic system (Gama Jr., 1979); a transition from marine to lacustrine settings (Castro & Medeiros, 1980); lacustrine to fluvial settings with associated aeolian deposits (Lavina, 1991; Rohn, 1994); a fluvio-deltaic system (Warren et al., 2008); and distributive fluvial systems (Schemiko et al., 2014; Manna, 2024).

Current paleoenvironmental and paleogeographic reconstructions of the Rio do Rasto Formation, as proposed by Manna (2024), point to distributive fluvial systems fed by distinctive drainage basins. These systems consisted of basal lacustrine deposits overlain by fluvial, overbank, and aeolian deposits. Toledo (2023) also details the interaction between fluvial and aeolian processes at different frequencies and magnitudes. Together, these studies demonstrate the architectural complexity of the stratigraphic framework of continental sedimentary successions.

3. Materials and Methods

The samples used in this study were obtained from drill cores provided by SGB (Geological Survey of Brazil), collected in the municipalities of Rio Pardo and Taquara, in the state of Rio Grande do Sul (**Figure 1**). Fifteen representative samples of the different sedimentary facies present were selected (**Figure 2** and **Figure 3**), aiming for a comprehensive characterization of the pore system. The samples were subjected to three main analytical techniques:

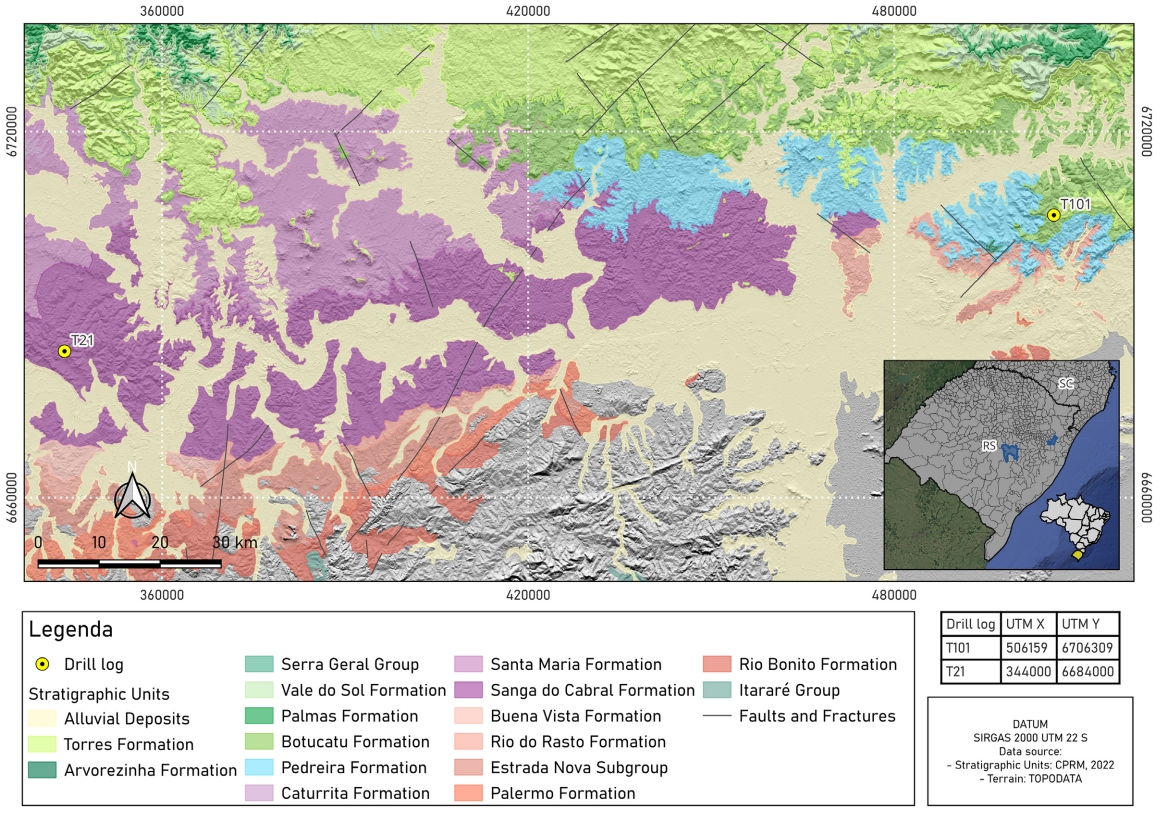

Figure 1. Geological and location map of the drill logs used. Eight samples were collected from core T21, located in the municipality of Rio Pardo, and seven from core T101, located in the municipality of Taquara.

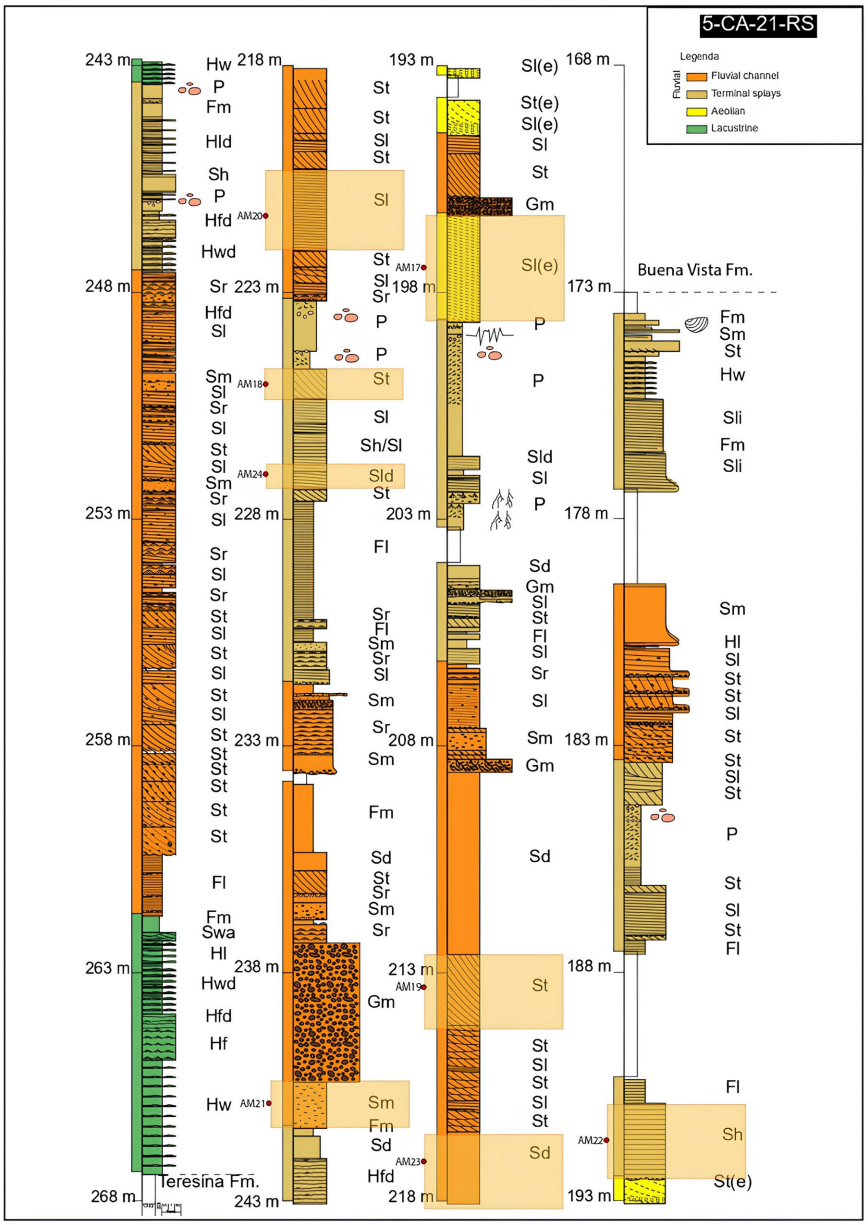

Figure 2. Composite sections of drill log T21 based on the sedimentological and stratigraphic data described by Manna (2024) and Toledo (2023), showing the collected samples.

1) Thin section analysis for petrographic characterization and identification of diagenetic processes;

2) X-ray computed microtomography (micro-CT) to obtain images of the internal pore structure;

3) Mercury intrusion porosimetry (MIP) to determine porosity, pore size distribution, and permeability characteristics.

Analyses 1 and 2 were performed on all 15 samples (**Table 1**), while analysis 3 was conducted on a subset of 4 samples. The selection of samples for MIP was to enhance the comprehension of possible microporosity, due to the limitations in the resolution of the obtained images from micro-CT.

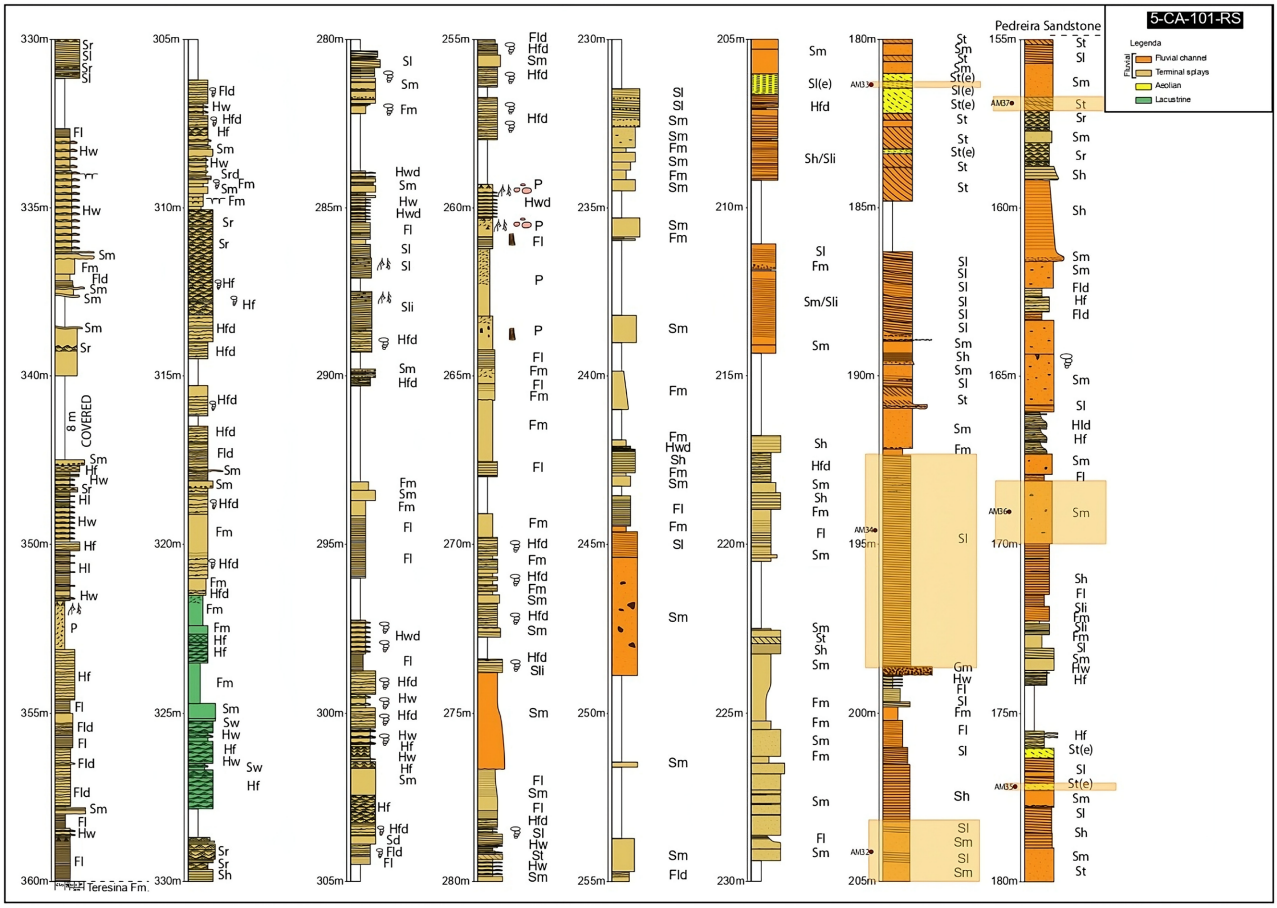

Figure 3. Composite sections of drill log T101 based on the sedimentological and stratigraphic data described by Manna (2024) and Toledo (2023), showing the collected samples.

Table 1. Characterization of sandstones according to subsystems based on Manna (2024) and Toledo (2023) of the samples used in the study.

Sample	Subsystem	Facies Association	Facies
T21AM17	Eolian deposits	Eolian sandsheets	Sl(e)—Eolian sandstones with low-angle cross-lamination/cross-stratification
T21AM18	Overbank Deposits	Terminal splays	Sti—Sandstones with incipient tangential cross-stratification
T21AM19	Fluvial channel deposits	Lateral accretion bars	St—Sandstones with tangential cross-stratification
T21AM20	Fluvial channel deposits	Aggradational sandy bedforms	Sl—Sandstones with low-angle cross-lamination/cross-stratification
T21AM21	Fluvial channel deposits	Aggradational sandy bedforms	Sm—Massive sandstones
T21AM22	Overbank Deposits	Terminal splays	Sh—Sandstones with horizontal laminations/stratifications
T21AM23	Fluvial channel deposits	Aggradational sandy bedforms	Sd—Sandstone with predominant planar cross-stratification
T21AM24	Overbank Deposits	Terminal splays	Sld—Sandstone with deformed low-angle cross-stratification
T101AM31	Eolian deposits	Eolian dunes	St(e)—Eolian sandstones with tangential cross-stratification

Continued

T101AM32	Fluvial channel deposits	Aggradational sandy bedforms	Sm/Sli—Massive sandstones/Sandstones with incipient low-angle cross-lamination/stratification
T101AM33	Eolian deposits	Eolian dunes	Sl(e)—Eolian sandstones with low-angle cross-stramination/cross-stratification
T101AM34	Fluvial channel deposits	Aggradational sandy bedforms	Sl—Sandstones with low-angle cross-lamination/cross-stratification
T101AM35	Eolian deposits	Eolian dunes	St(e)—Eolian sandstones with tangential cross-stratification
T101AM36	Fluvial channel deposits	Aggradational sandy bedforms	Sm—Massive sandstones
T101AM37	Fluvial channel deposits	Lateral accretion bars	St—Sandstones with tangential cross-stratification

3.1. Petrographic Analysis

Petrographic thin section preparation was outsourced to the specialized company Petrografia BR, the samples were impregnated with blue epoxy for better visualization of the pore system. Subsequent petrographic analysis was conducted using an Olympus BX 41 optical microscope. This equipment enabled the description of the main mineralogical constituents and textural aspects of the samples, including mineral identification, types and distribution of porosity, grain size, types of intergranular contacts, cement nature, matrix presence, and evidence of diagenetic processes.

The adopted analytical method was point counting, with 300 points registered per thin section. The generated data was subsequently compiled and processed in Microsoft Excel spreadsheets. The samples were compositionally classified according to Folk (1968).

3.2. X-Ray Computed Microtomography

X-ray computed microtomography (Micro-CT) was used for three-dimensional characterization of the samples pore structure. This non-destructive technique is based on the principle of X-ray beam attenuation as it interacts with matter. Variations in material density and composition result in differences in attenuation coefficients, generating contrast that enables distinction between the solid matrix and pore spaces (Neto et al., 2011; Porto, 2015).

For the analysis, specimens were prepared as mini-plugs with approximate dimensions of 3 mm in diameter and 9 mm in height at the Porous Media and Thermophysical Properties Laboratory (LMPT/UFSC). Data acquisition was performed using a Zeiss Versa XRM-500 microtomograph.

Tomographic data post-processing involved three-dimensional reconstruction and quantitative analysis of the pore structure. The Avizo 3D software was employed for generating three-dimensional models, and calculating the porosity and permeability values while the C3DE software was used specifically for pore network and throat extraction. A fundamental step in this process was image binarization, where the application of a threshold (T) enabled digital segmentation of the image into two phases: solid matrix and pore space (Sonka et al., 2013). To optimize this

segmentation, Non-Local Means and unsharp masking filters were applied. This procedure facilitated the quantification of microstructural parameters such as porosity, connectivity, and pore size distribution.

3.3. Mercury Intrusion Porosimetry

Mercury intrusion porosimetry (MIP) was performed on four samples prepared as cubes with approximately 1 cm edges. The method is based on the principle that mercury, being a non-wetting fluid, requires the application of external pressure to penetrate the sample's pores (Kronbauer, 2014). The relationship between the applied pressure and pore radius is governed by the Washburn equation.

The test enables determination of effective porosity (ϕ) through the ratio between the volume of mercury intruded into the connected pores (Vp) and the total sample volume (Vt), according to the equation:

$$\phi = Vp / Vt$$

In addition to porosity, the method provides pore throat size distribution derived from the curve of intruded volume versus applied pressure.

4. Results

4.1. Petrographic Analyses

The petrographic analyses performed on samples from the Morro Pelado Member revealed four types of sandstones (Table 2). Drill log 21 proved to be much richer in quartz, whereas drill log 101 showed a much greater abundance of lithic grains and feldspars (Figure 4).

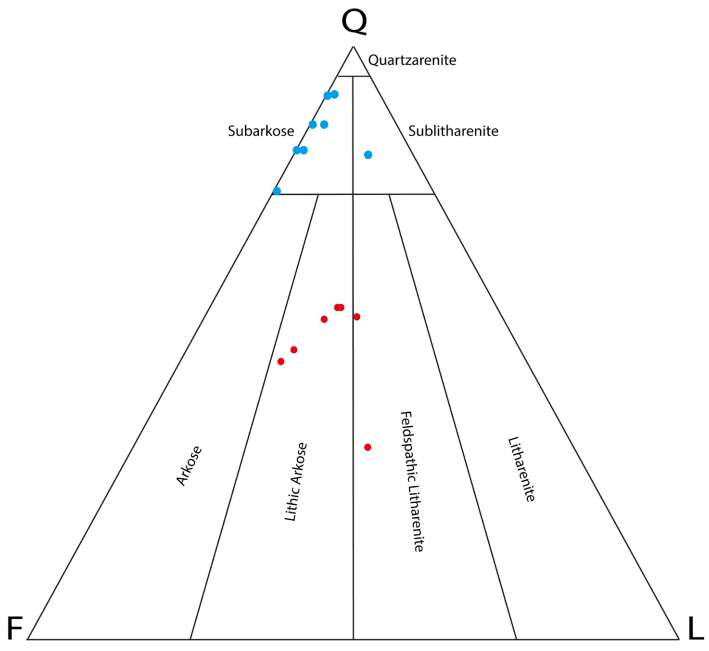

Figure 4. Framework composition of 15 samples from the Morro Pelado Member. Plotted on the Folk (1968) ternary diagram. In blue, samples from drill log 21; in red, samples from drill log 101.

Table 2. Percentage of porosity, quartz, feldspar, lithics and depth per sample.

Sample	Q (%)	F (%)	L (%)	Rock type	Porosity (%)	Depth
T21AM17	75.54	24.46	0	Subarkose	18.3	198 m
T21AM18	91.67	8.33	0	Subarkose	28.3	225 m
T21AM19	81.74	17.39	0.87	Subarkose	31.7	213 m
T21AM20	86.09	11.3	2.61	Subarkose	33.3	221 m
T21AM21	81.48	7.41	11.11	Sublitharenite	26	240 m
T21AM22	86.84	13.16	0	Subarkose	0.33	192 m
T21AM23	90.48	7.94	1.58	Subarkose	32.7	218 m
T21AM24	81.48	16.67	1.85	Subarkose	17.3	227 m
T101AM31	56	24	20	Lithic Arkose	13.6	173 m
T101AM32	55.86	24.32	19.82	Lithic Arkose	15.3	202 m
T101AM33	53.85	27.35	18.8	Lithic Arkose	16.7	180 m
T101AM34	54.33	22.05	23.62	Feldspathic Litharenite	24.7	195 m
T101AM35	32.48	31.62	35.9	Feldspathic Litharenite	26	175 m
T101AM36	48.74	34.45	16.81	Lithic Arkose	26.3	168 m
T101AM37	46.81	37.59	15.6	Lithic Arkose	19.7	156 m

4.1.1. Eolian Deposits Subsystem

Sandsheets have a total porosity of 18.3%, as observed in thin section. This porosity is predominantly primary intergranular, accounting for 70.9% of the total. The grains are fine to medium-grained, with shapes ranging from subangular to subrounded. Intergranular contacts are mostly long. Silica cement occurs locally, distributed sparsely within the rock framework without causing significant obstruction of the pore system. The mineral assemblage is dominated by quartz grains, accompanied by feldspars and oxides (Figure 5(A)).

Eolian Dunes exhibit more variable porosity (13% - 26%) in thin section, with notable development of secondary intragranular porosity (10% - 63%), evident in moldic pores and dissolved grains (Figure 5(B)). The grains are typically more rounded and establish elongated and point contacts. Mineralogically, quartz, feldspars, and oxides (24% - 44%) are observed, forming coatings around the grains (Figure 5(C)). Carbonate cement (4% - 8%) partially fills the pore spaces (Figure 5(D)).

4.1.2. Fluvial Channel Deposits

Lateral Accretion Bars exhibit total porosity ranging from 20% to 32%, as observed in thin section, with a predominance of primary intergranular porosity, accounting for 50% to 79% of the total identified pore volume. The grains show textural variation from subrounded to subangular, with intergranular contacts ranging from long to point contacts. The mineral assemblage is primarily composed of quartz, feldspars, and oxides (Figure 5(E)). Carbonate cement occurs subordinately, representing approximately 1% of the total rock volume (Figure 5(F)). Aggradational Sandy Bedforms are characterized by high porosity, ranging from 15% to 33%, as observed in thin section. The predominant porosity in these

sandstones corresponds to primary intergranular pores, accounting for 13% to 85% of the total (Figure 5(G) and Figure 5(H)). In turn, secondary intragranular pores (Figure 6(A)) are more developed in facies composed of massive sandstones and sandstones with incipient laminations or low-angle cross-stratification, representing 24% to 52% of the porosity in these lithofacies. Texturally, the sandstones exhibit good grain-size sorting, with the frequent occurrence of elongated to concave-convex intergranular contacts (Figure 6(B)). Cement is observed subordinately and dispersed (Figure 6(C)), insufficient to significantly obstruct the pores. Additionally, the presence of intraclasts dispersed within the sedimentary framework is recorded (Figure 6(D)).

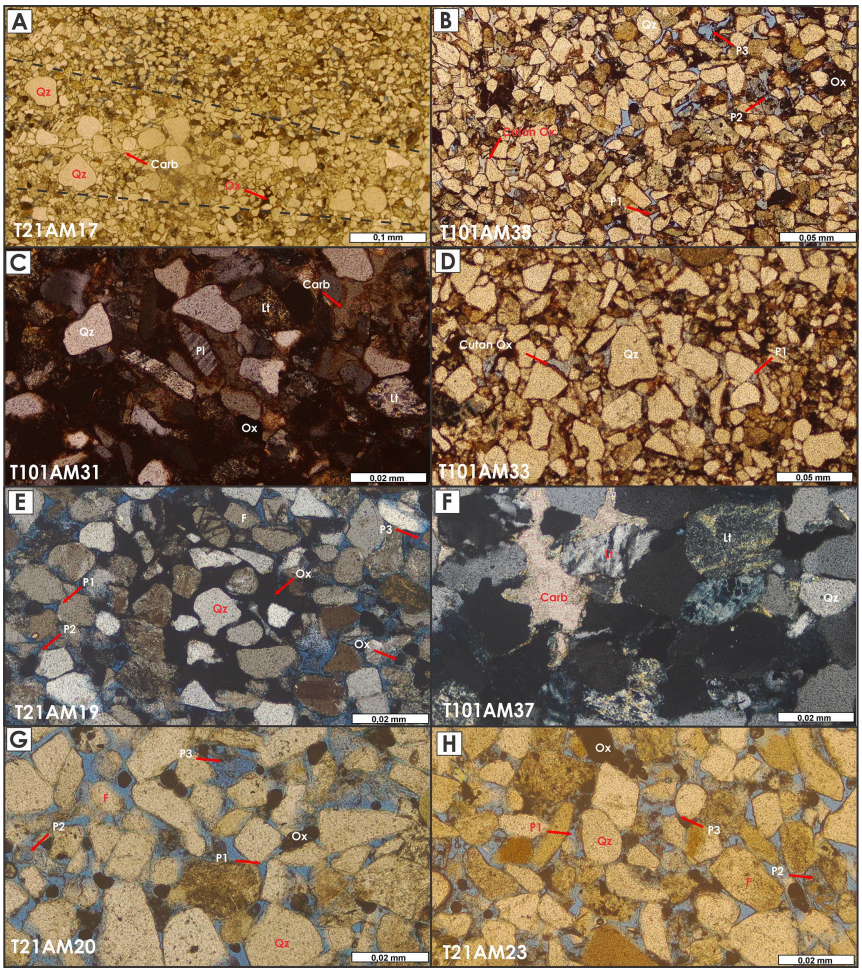

Figure 5. Qz: Quartz, F: Feldspar, Pl: Plagioclase, Ox: Oxides, Lt: Lithics, Carb: Carbonate Cement, P1: Primary intergranular porosity, P2: Secondary intragranular porosity, P3: Moldic porosity. (A) Sample showing granulometric (grain-size) variation. (B) Sample with oxide cutans. (C) Sample with presence of lithic grains, plagioclase, oxides, and carbonate cement (cross-polarized light). (D) Sample with oxide cutans and primary intergranular porosity. (E) Sample exhibiting three types of porosity, along with aggregation of oxides forming cement. (F) Sample with presence of carbonate cement and lithic grains (cross-polarized light). (G) Sample with high primary intergranular porosity, presence of moldic porosity, long and point contacts, and aggregation of oxides. (H) Sample with high primary intergranular porosity and oxide globules.

4.1.3. Overbank Deposits

Terminal Splays composed of sandstones with incipient tangential cross-stratification exhibit the highest primary intergranular porosity in the system (96%) (Figure 6(E)). The predominantly subrounded grains have contacts ranging from long to point contacts. Cement is scarce, and the mineralogical composition is marked by extremely abundant quartz (78%), with small amounts of feldspars (8%) and oxides (9%).

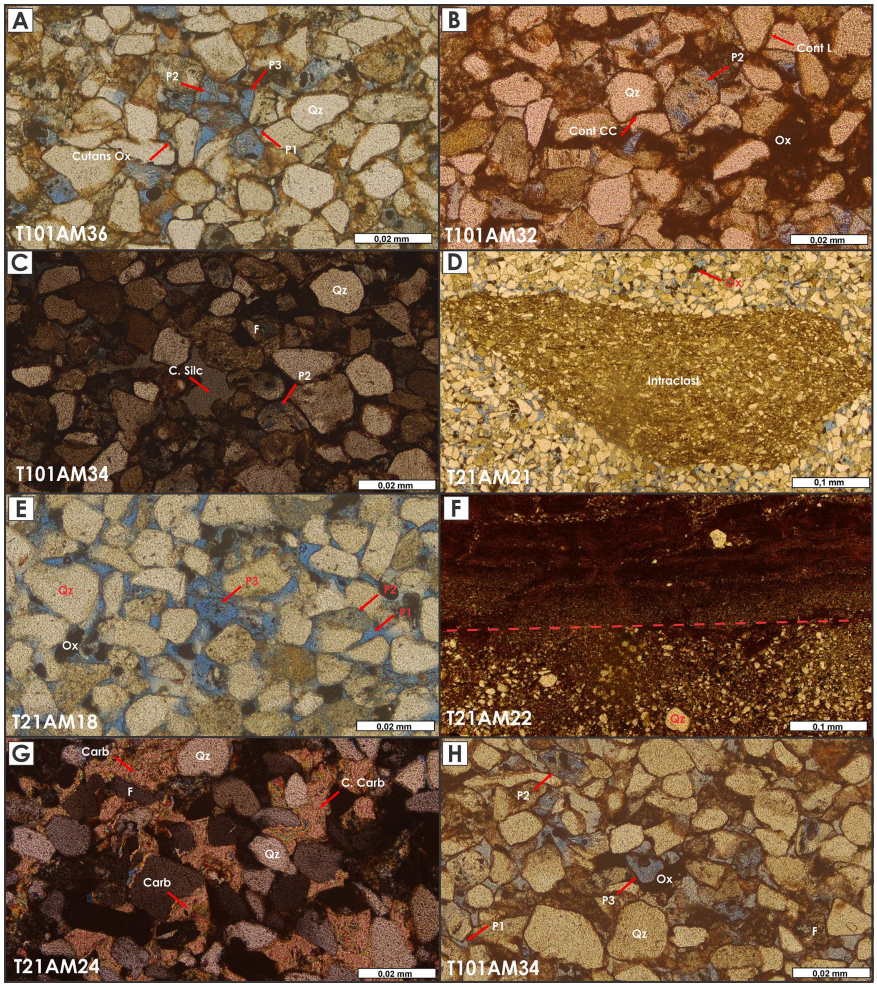

Figure 6. Qz: Quartz, F: Feldspar, Pl: Plagioclase, Ox: Oxides, Lt: Lithics, Carb: Carbonate Cement, C. Silc: Silica Cement, P1: Primary intergranular porosity, P2: Secondary intragranular porosity, P3: Moldic intragranular porosity. (A) Secondary and moldic intragranular porosity, with grains showing concave-convex contacts. (B) Sample with secondary intragranular porosity and concave-convex contacts. (C) Sample with pinpoint silica cement and presence of intragranular dissolution porosity (cross-polarized light). (D) Sample with predominance of primary intergranular porosity and an intraclast. (E) Sample with oxide cutans and moldic intragranular porosity. (F) Sample with an abundance of clay matrix, with grain-size variation up to sand-sized grains. (G) Sample with high content of carbonate cement and oxides (cross-polarized light). (H) Sample with oxide cutans and moldic intragranular porosity.

Horizontally Laminated Deposits are notable for the near absence of porosity

due to an abundant clay matrix (70%) (Figure 6(F)). The grains, which range from subrounded to subangular, are enveloped in a fine mass of clay minerals. The mineralogy includes quartz, micas, and oxides (15%).

In Sandstones with Deformed Stratification, the moderate porosity (17%) shows a mixed distribution: 73% primary intergranular, 19% dissolution porosity, and 8% moldic porosity. The subangular to angular grains establish mainly long contacts with some point contacts. Carbonate cement and a significant presence of oxides (41%) are notable (Figure 6(H)).

4.2. Petrophysical Parameters

The obtained petrophysical parameters revealed multi-scale porous systems (Table 3 and Table 4), whose characterization required the integration of complementary techniques. Micro-CT analyses, while essential for evaluating macroporosity (above ~4 μm), had limitations in detecting pores below their resolution, underestimating the total porosity in samples with fine matrix or significant microporosity. Mercury intrusion porosimetry (MIP) demonstrated the presence of a considerable fraction of micropores, increasing the total porosity values compared to micro-CT data. However, even with fair to good porosity (13.84% - 18.07%), the permeability in these systems was low to moderate (0.34 - 23.87 mD), reflecting the critical influence of pore connectivity at reduced scales.

Table 3. Petrophysical parameters obtained from the binarization of micro-CT images.

Sample	Facies Association	Resolution (μm)	Porosity (%)	Permeability (mD)		
				Eixo X	Eixo Y	Eixo Z
T21AM17	Eolian Sandsheets	4.33	5.471	8.89	4.85	0.00
T21AM18	Terminal Splays	3.96	25.527	2.428.44	1.787.80	2.151.14
T21AM19	Lateral Accretion Bars	4.36	21.387	874.35	563.50	502.51
T21AM20	Aggradational Sandy Bedforms	4.24	14.390	22.33	48.40	79.10
T21AM21	Aggradational Sandy Bedforms	4.05	17.259	258.34	232.43	143.93
T21AM22	Terminal Splays	4.47	0.330	0.00	0.00	0.00
T21AM23	Aggradational Sandy Bedforms	3.87	21.955	1.299.48	1.099.62	616.84
T21AM24	Terminal Splays	3.79	0.905	0.00	0.00	0.00
T101AM31	Eolian Dunes	4.57	3.222	0.00	0.00	0.00
T101AM32	Aggradational Sandy Bedforms	4.47	3.781	0.00	0.00	0.00
T101AM33	Eolian Dunes	4.05	5.441	0.00	0.00	0.00
T101AM34	Aggradational Sandy Bedforms	4.57	3.962	0.00	0.00	0.00
T101AM35	Eolian Dunes	4.37	5.760	3.71	0.00	0.00
T101AM36	Aggradational Sandy Bedforms	4.47	2.934	0.00	0.00	0.00
T101AM37	Lateral Accretion Bars	4.47	3.449	0.00	0.00	0.00

Table 4. Petrophysical parameters obtained from MIP.

Samples	Facies Association	Porosity (%)	Permeability (mD)	Pore Diameter (μm)
T21AM17	Eolian Sandsheets	15.17	2.77	0.04
T21AM22	Terminal Splays	16.2	23.87	0.03
T21AM24	Terminal Splays	13.84	3.21	0.02
T101AM32	Aggradational Sandy Bedforms	18.07	0.34	0.06

4.2.1. Eolian Deposits

The sandstones associated with eolian sandsheets exhibited a total porosity around 15%, with permeability on the order of 2.7 mD and an average pore diameter of approximately 0.04 μm, as determined by mercury intrusion porosimetry. Data obtained by microtomography revealed a lower effective porosity, of approximately 5%, in addition to evidencing anisotropy in permeability, with values ranging between 8.9 mD and 4.8 mD along two of the analyzed axes (Figure 7(A)).

In the sandstones from eolian dunes, the results indicated porosity below 6%, associated with an absence of detectable permeability within the resolution scale of microtomography (Figures 7(A)-(C)). It is noteworthy that the low-angle laminations and cross-stratifications, typical of the eolian depositional process, could be recognized in the three-dimensional models of pore networks and throats (Figure 7(C)), indicating the influence of the depositional structure on the organization of the pore space.

4.2.2. Fluvial Channel Deposits

The sandstones associated with lateral accretion bars reveal discrepant porosities, ranging from 21.38% to 3.45% (Figure 8(A) and Figure 9(D)). The permeability in the more porous facies proved to be anisotropic, varying from 502.51 mD to 874.35 mD along different axes. In contrast, permeability in the less porous facies was negligible (effectively zero) due to the resolution limit of the equipment used.

The aggradational sandy bedforms exhibit a marked variability in their petrophysical properties, revealing two distinct behavioral patterns. The first group shows favorable characteristics, with porosities ranging from 14.39% to 21.96%, associated with significant permeabilities reaching up to 1299.48 mD (Figures 8(B)-(D)). These values correspond to deposits with low-angle cross-stratification, planar stratification, and massive sandstones.

In contrast, the second group shows more restrictive properties, with porosities between 2.93% and 3.96% and permeabilities below the resolution limit (Figures 9(A)-(C)). However, complementary analyses by Mercury Intrusion Porosimetry (MIP) revealed a microporous structure not previously detected, particularly in massive sandstones with incipient cross-laminations, which showed 18.07% porosity. Despite this considerable value, permeability remained low (0.34 mD), suggesting that the pores, although numerous, have limited connectivity.

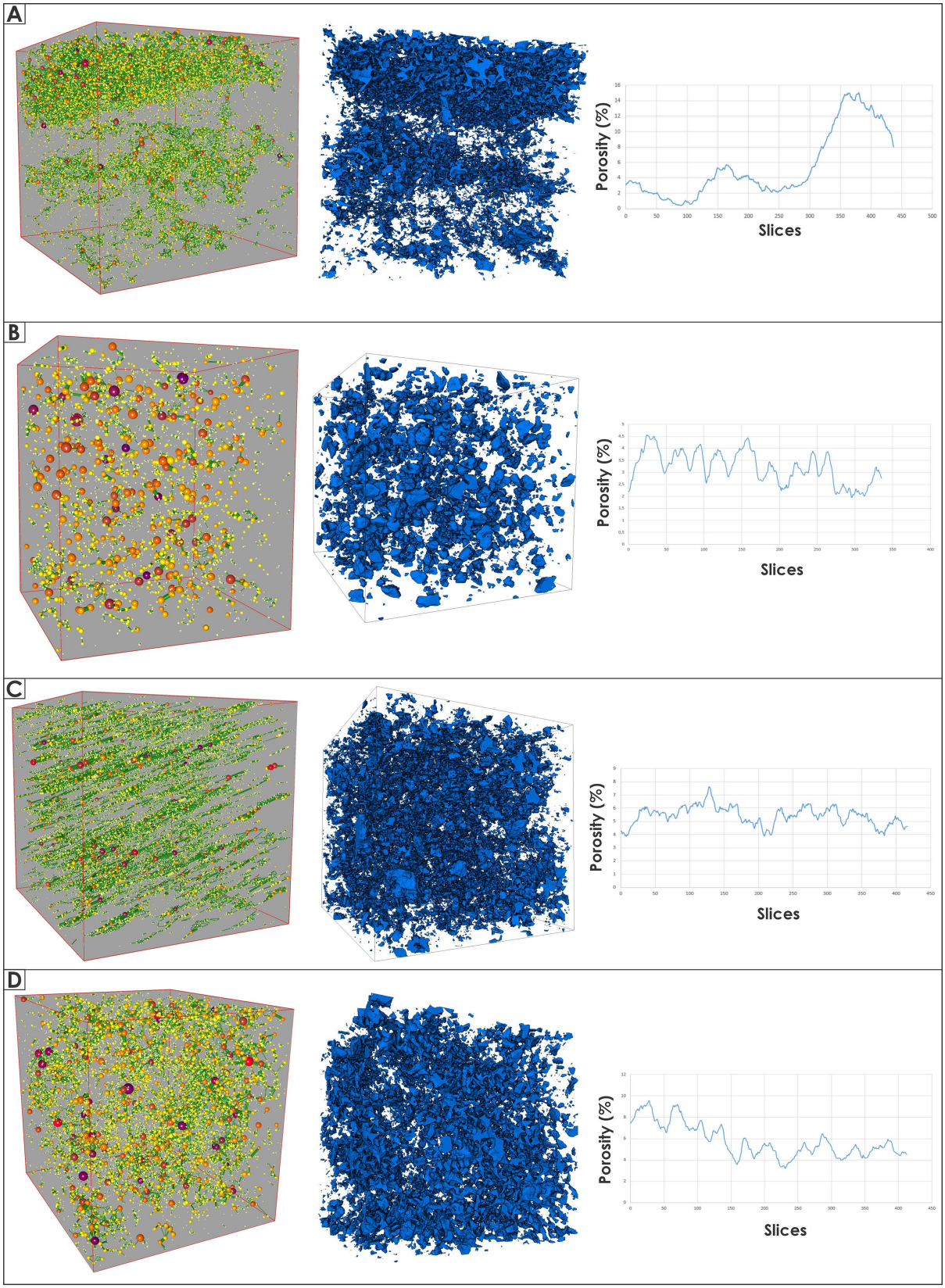

Figure 7. Pore network and throat models, 3D models and porosity distribution from the eolian deposits. (A) Eolian Sand-sheet sample; (B) (C) (D) Eolian dunes samples.

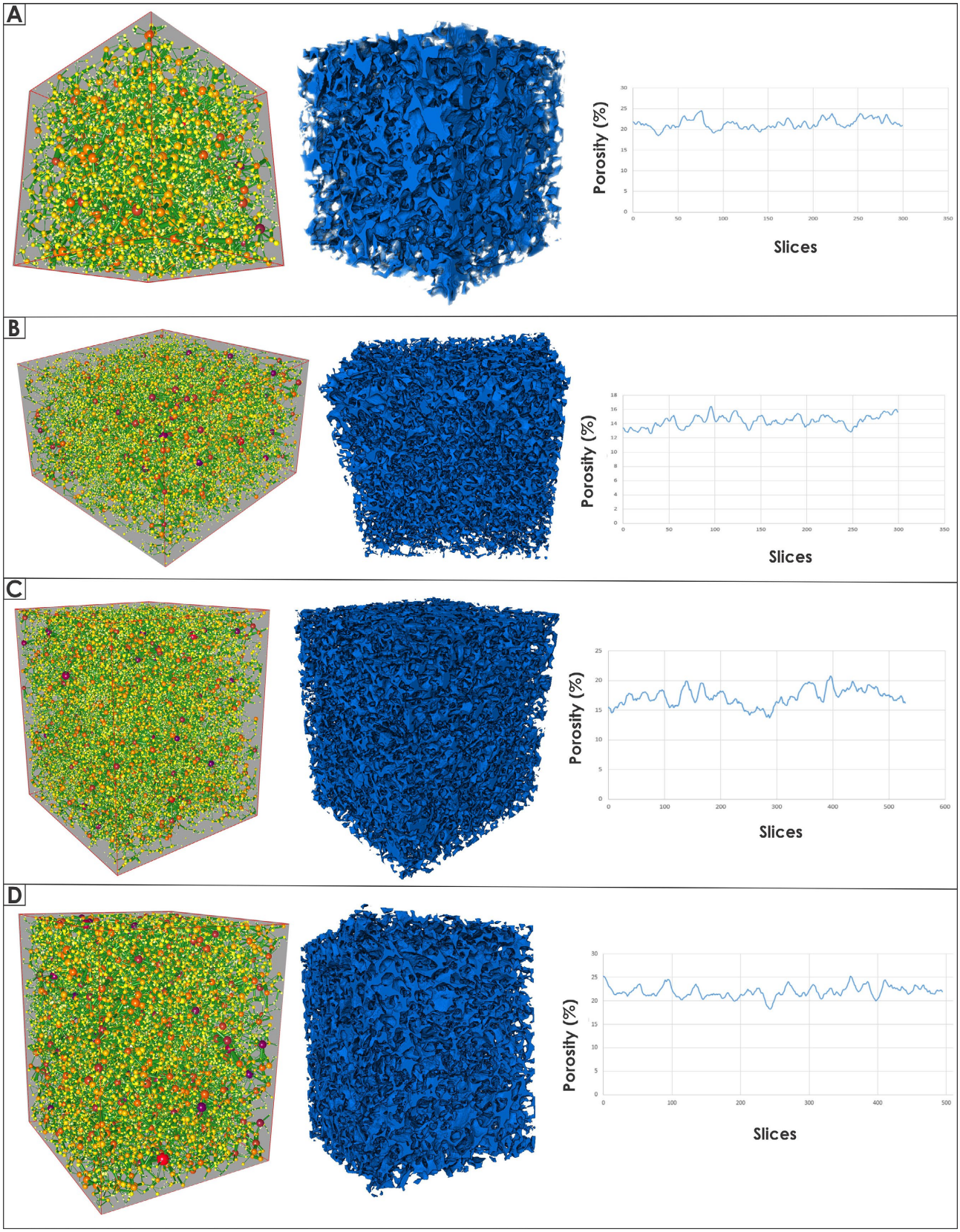

Figure 8. Pore network and throat models, 3D models and porosity distribution from the fluvial channel deposits of the core sample 21. (A) Lateral accretion bars sample; (B) (C) (D) Aggradational sandy bedforms samples.

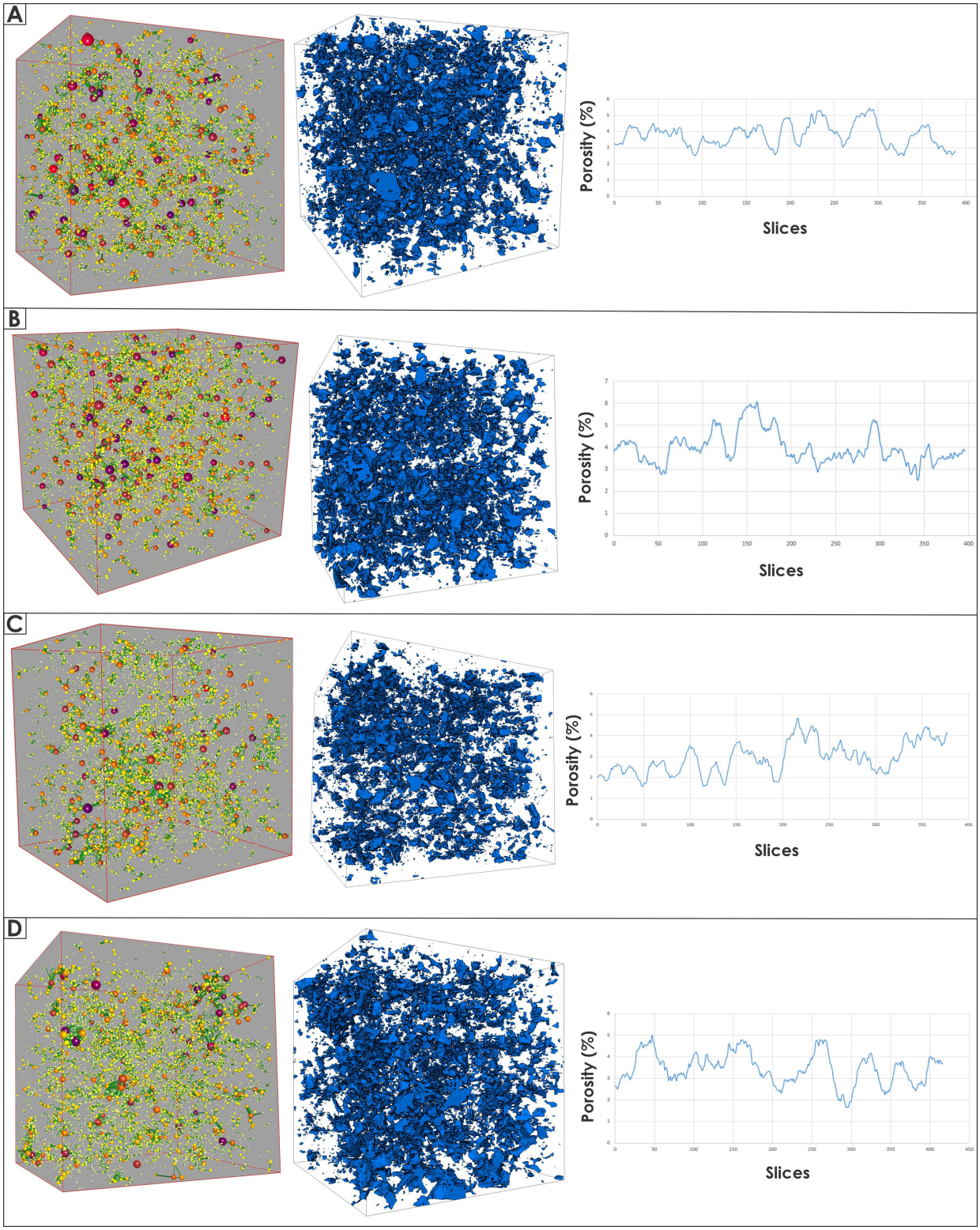

Figure 9. Pore network and throat models, 3D models and porosity distribution from the fluvial channel deposits of the core sample 101. (A) (B) (C) Aggradational sandy bedforms; (D) Lateral accretion bars.

4.2.3. Overbank Deposits

The sandstones associated with terminal splays revealed three distinct porosity-

permeability behaviors. Deposits with incipient tangential cross-stratification present the most favorable properties, with a porosity of 25.53% and permeabilities ranging between 1787.80 mD and 2428.44 mD along the different axes of analysis (Figure 10(A)).

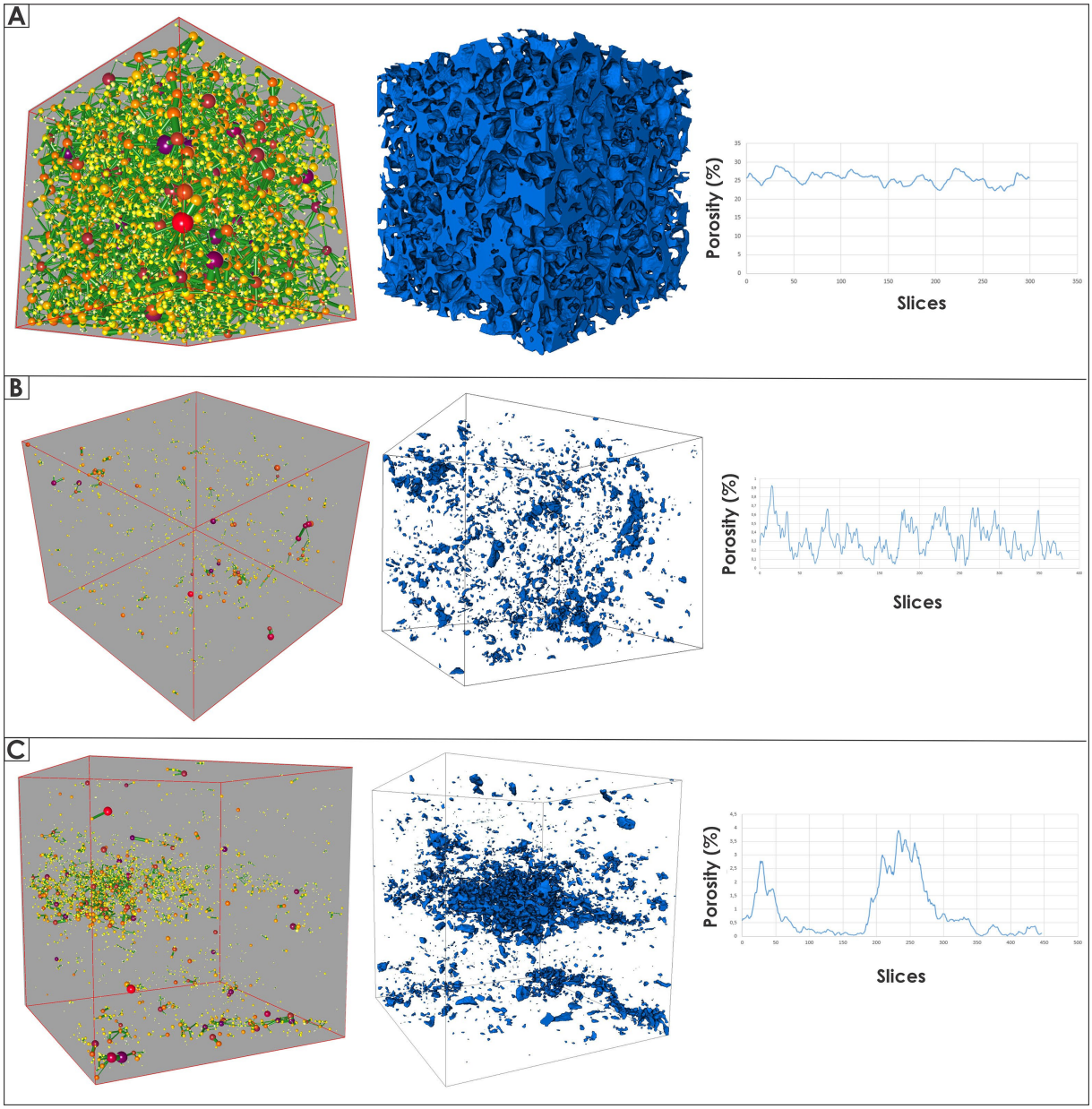

Figure 10. Pore network and throat models, 3D models and porosity distribution from the overbank deposits. (A) (B) (C) Terminal splays samples.

In contrast, deposits with horizontal laminations show radically different characteristics (Figure 10(B)). Micro-CT scanning registered only 0.33% porosity, while Mercury Intrusion Porosimetry (MIP) revealed higher values (16.2% porosity and 23.87 mD permeability), with an average pore throat diameter of 0.03 μm. This discrepancy indicates the presence of microporosity below the resolution

threshold of the micro-CT scan.

Finally, deposits with deformed cross-stratification presented an intermediate behavior. Micro-CT analysis showed 0.905% porosity, contrasting with the 13.84% obtained by MIP, which also revealed a permeability of 3.21 mD and an average pore throat diameter of 0.02 μm (**Figure 10(C)**).

5. Discussion

The integrated analysis of petrographic, microtomographic, and porosimetry data reveals a strong correlation between the depositional architecture of the Morro Pelado Member, as proposed by Manna (2024), and its resulting petrophysical properties. The heterogeneity observed in the pore systems is not random but fundamentally controlled by the distinct sedimentary processes and subsequent diagenetic history inherent to each depositional subsystem. This discussion will detail these correlations, explaining the petrophysical behavior of each facies association within its sedimentological context.

5.1. Eolian Deposits Subsystem: The Microporous, Low-Connectivity Reservoirs

While eolian deposits commonly exhibit higher porosity and permeability, this generalization requires careful application to systems significantly influenced by water-related processes (Bofill et al. 2025). The eolian deposits, comprising eolian sandsheets and eolian dunes, consistently behave as low-permeability reservoirs, a characteristic directly linked to their depositional and post-depositional evolution.

Eolian Sandsheets as described by Manna (2024) form as thin, extensive sheets in wet interdune areas. The sample T21AM17 reflects this environment, showing good total porosity (~15% by MIP) dominated by primary intergranular pores (70.9%). The good initial sorting typical of eolian transport created a well-defined pore network. However, the permeability is strikingly low (2.77 mD). The observed discrepancy between good porosity and low permeability is best explained by a combination of early diagenetic processes. While primary intergranular pores are preserved and grain dissolution created significant secondary porosity, carbonate cementation occluded the connecting pore throats. The isolated pores, initiated within feldspars, as proposed by Monsees et al. (2021) for Permian Rotliegend sandstones, likely commenced prior to deposition and progressed throughout early diagenesis, persisting until the diminishing influence of meteoric waters during burial diagenesis. Preserving porosity but severely reducing connectivity and effective permeability. Furthermore, the permeability anisotropy detected by micro-CT analysis (8.89 mD vs. 4.85 mD) can be attributed to subtle, low-angle lamination (**Figure 5(A)**) within this facies, which imparts a preferred orientation and heterogeneous flow pathways to the pore system, as observed in **Figure 7(A)**.

Eolian Dunes in contrast to the eolian sandsheets, show a more homogeneous

pore system as observed in the porosity distribution graphs in **Figures 7(B)-(D)**. While primary intergranular porosity is present, there is a notable development of secondary intragranular and moldic porosity (up to 63% of the total porosity in some samples). This is a classic signature of dissolution processes, developed during diagenesis through the dissolution of detrital and diagenetic constituents (De Ros, 1990). Furthermore, the presence of carbonate cement (4% - 8%) partially occludes pores. The model of Manna (2024) for wet eolian dunes suggests a high water table, which would favor such early diagenetic like dissolution. The combination of isolated secondary pores and pore-filling cement results in a system with low effective connectivity, explaining why micro-CT shows very low permeability (often below detection limit). One of the 3D models captures the inherited eolian cross-stratification, indicating that the depositional architecture dictates the fundamental skeleton of the pore network. This is consistent with the findings of Maithel et al. (2021), who notes that high-resolution scans provide a detailed representation of cross-beds.

5.2. Fluvial Channel Deposits Subsystem: High-Quality But Anisotropic Reservoirs

This subsystem, represented by lateral accretion bars and aggradational sandy bedforms, contains the most prolific reservoirs in the study, aligning with their interpretation as high-energy channel deposits by Manna (2024).

Lateral Accretion Bars form by the lateral migration of meandering channels (Manna, 2024). Samples like T21AM19 exhibit high porosity (21.39%) and, crucially, very high and anisotropic permeability (e.g., 874 mD vs. 503 mD). One of the factors for high porosity can be explain by the type of rock, several authors have observed that subarkoses sometimes exhibit a greater potential for porosity preservation than quartzarenites. According to Bjørlykke et al. (1989), the presence of feldspars inhibits the extensive development of quartz cement. This observation is supported by Parnell (1987), who, in a study of Paleozoic sandstones from Wales, identified subarkoses as the composition with the most favorable porosity preservation potential. The petrography confirms a clean sandstone with well-developed primary intergranular porosity and minimal cement.

Aggradational Sandy Bedforms shows the highest variability, reflecting a range of flow regimes within the channel system. Well-sorted sandstones with low-angle or planar cross-stratification (e.g., T21AM20, T21AM23) exhibit excellent properties (porosity >17%, permeability >1000 mD). Their textural maturity, with point and long contacts, and well-preserved intergranular porosity, leads to a well-connected macroporous system.

In contrast, the massive to incipiently stratified sandstones (Sm/Sli), exemplified by sample T101AM32, present a petrophysical divergence. While micro-CT analysis reveals low porosity and negligible permeability, MIP detects a significant microporous system, with a porosity of 18.07%. This microporosity (0.06 μm average pore diameter) could be attribute to the dissolution of grains as suggested

by Shanmugan (1985). However, it is poorly interconnected, resulting in the observed very low permeability of 0.34 mD. The high total porosity is largely reflective of the 52% moldic porosity, which, being isolated, explains the low connectivity and consequent low permeability.

5.3. Overbank Deposits Subsystem: The Division between Seal and Reservoir

The overbank deposits exhibits the most significant contrasts in reservoir quality, serving as a prime example of how subtle facies variations govern petrophysical behavior. As interpreted by Manna (2024), the characteristics of these deposits are governed by the interaction of flood event frequency and intensity, topographic depressions, and drainage configuration.

Terminal Splays—High-Quality Facies: These deposits represent by sample T21AM18 (Sti), present an exceptional porosity (25.53%) and permeability (>1700 mD). This characteristics can be explain by the near-absence of matrix and cement that allowed for the preservation of an unspoiled, highly connected intergranular pore network. This facies shows a more homogeneous porosity distribution (**Figure 10(A)**) and acts as high-permeability flow path. As noted by De Ros (1990), the abnormal pore-fluid pressures generated during rapid sedimentation can inhibit compaction and cementation, thereby preserving primary porosity.

Terminal Splays—Low-Quality Facies: Other splay deposits tell a completely different story. The horizontally Laminated Sandstones are dominated by a clay matrix (up to 70%), which completely occludes the primary porosity. Micro-CT rightly detects near-zero porosity and permeability. The significant porosity (16.2%) and moderate permeability (23.87 mD) revealed by MIP are attributed to a network of micropores within the clay matrix itself. This facies functions as a baffle or seal.

Sandstones with Deformed Stratification shows an intermediate character. The deformation processes may have disrupted the original fabric, reducing macroporosity (0.9% in micro-CT). However, the presence of dissolution and moldic porosity (27% of the total porosity in thin section) and a lower clay content than facies Sh creates a system with fair MIP porosity (13.84%) and low but measurable permeability (3.21 mD). The low permeability can be the result of the heterogeneous system within this facies, as observed in **Figure 10(C)**.

6. Conclusion

In conclusion, this integrated analysis demonstrates that the reservoir quality heterogeneity within the Morro Pelado Member is a direct consequence of its depositional architecture and the resultant diagenetic overprint. The distinct petrophysical character of each facies association is not merely incidental but is fundamentally dictated by the interplay of primary sedimentary processes and subsequent diagenetic pathways.

The Eolian Subsystem, comprising sandsheets and dunes, functions as a mi-

croporous system with low connectivity. Despite good initial porosity, its reservoir potential is severely compromised by diagenetic processes—primarily carbonate cementation occluding pore throats and the development of isolated secondary porosity—resulting in strikingly low permeability, even in the presence of significant total porosity.

The Fluvial Channel Subsystem contains the most prolific reservoirs, characterized by high porosity and permeability. Their quality is governed by textural maturity, the preservation of a well-connected intergranular pore network, and in some cases, a subarkosic composition that inhibits quartz cementation. However, their performance is anisotropic, influenced by depositional structures like lateral accretion surfaces.

The Overbank Subsystem presents the most dramatic petrophysical duality, perfectly encapsulating the control exerted by subtle facies variations. Here, the stark contrast between high-permeability conduits (clean terminal splays) and effective seals/clay-rich baffles is a direct function of depositional energy, sediment sorting, and clay matrix content, illustrating a definitive continuum from reservoir to non-reservoir rock within a single genetic environment.

Collectively, these subsystems form a composite aquifer where the primary hydraulic function of each is determined by its depositional origin: Fluvial Channels constitute the high-transmissivity core, Overbank deposits create a complex system of seals and localized pathways, and Eolian deposits form hydraulically restrictive units.

Ultimately, this study confirms that a predictive model for reservoir behavior in the Morro Pelado Member must be grounded in a detailed understanding of its sedimentological framework. The petrophysical properties are an intrinsic signature of the depositional system, subsequently modified by a diagenetic history that is itself often a function of the primary depositional fabric.

To better understanding of the specific diagenetic reactions that govern porosity and permeability evolution, scanning electron microscopy (SEM) is recommended. Unlike the current methods, SEM would provide critical high-resolution, direct visualization of pore-throat-occluding cements, clay mineral morphology, and dissolution textures. This essential micro-scale data would uniquely identify the specific mineral phases and their spatial distribution, allowing for a more predictive model of reservoir quality evolution.

Acknowledgements

We extend our sincere gratitude to the Laboratory of Porous Media and Thermophysical Properties (LMPT) and the Reservoir Geology Laboratory (LGR) for their invaluable technical support and for providing the infrastructure necessary for this work. We are grateful to the Geological Survey of Brazil (SBG—Serviço Geológico do Brasil) for kindly supplying the core samples, which were essential to this research. This study was financially supported by the Santa Catarina State Foundation for Research and Innovation (FAPESC). The first author also acknowledges the

receipt of a scholarship from the Coordination for the Improvement of Higher Education Personnel (CAPES), which was fundamental for the completion of this work. We also thank the reviewers and the editorial team for their insightful comments and constructive suggestions, which significantly improved the quality of this manuscript.

Conflicts of Interest

The authors declare no conflicts of interest regarding the publication of this paper.

References

Bjørlykke, K., Ramm, M., & Saigal, G. C. (1989). Sandstone Diagenesis and Porosity Modification during Basin Evolution. *Geologische Rundschau, 78,* 243-268. https://doi.org/10.1007/bf01988363

Bofill, L., Bozetti, G., Schäfer, G., Ghienne, J., Schuster, M., Heap, M. J. et al. (2025). Sedimentary Control on Permeability Heterogeneity: The Middle Buntsandstein Continental Sandstones (Lower Triassic, Eastern France). *Marine and Petroleum Geology, 173,* Article 107261. https://doi.org/10.1016/j.marpetgeo.2024.107261

Castro, J. C., & Medeiros, R. A. (1980). Excursão 9: Fácies e modelos de sedimentação das Formações Rio do Sul e Rio Bonito, leste de Santa Catarina; fácies e evolução sedimentar do Grupo passa Dois na BR 470 SC. *Congresso Brasileiro de Geologia* 31 (pp. 69-97), SBG.

Dal Col, A. H., Gali, P. H., & Appoloni, C. R. (2016). Análise microestrutural de arenito da formação rio do rasto pela microtomografia computadorizada por raios x. *Semina: Ciências Exatas e Tecnológicas, 37,* 3-12. https://doi.org/10.5433/1679-0375.2016v37n2p3

De Ros, L. F. (1990). Preservação e geração de porosidade em reservató-rios clásticos profundos: Uma revisão. *Boletim de Geociências da PETROBRÁS, 4,* 387-404.

Descovi Filho, Leônidas Luiz, V., Scheibe, L. F., & Nanni, A. S. (2023). Compartimentação do sistema aquífero integrado guarani/serra geral em santa catarina em blocos geomorfoestruturais com uso de geotecnologia livres. *Geosul, 38,* 377-394. https://doi.org/10.5007/2177-5230.2023.e76101

Fernandes, J. S. (2009). *Caracterização microestrutural do espaço poroso de rochas reservatório da Bacia do Rio Tibagi por microtomografia de raios x.* Tese de Doutorado, Universidade Estadual de Londrina.

Gama Jr., E. (1979). A sedimentação do grupo passa dois (exclusive formação irati): Um modelo geomórfico. *Revista Brasileira de Geociências, 9,* 1-16. https://doi.org/10.25249/0375-7536.1979116

Gordon Jr., M. (1947). *Classificação das formações gonduânicas do Paraná, Santa Catarina e Rio Grande do Sul* (Vol. 38, p. 20). Notas preliminares e estudos DNPM-DGM.

Hirata, R., Suhogusoff, A. V., Marcellini, S. S., Villar, P. C., & Marcellini, L. (2019). *As águas subterrâneas e sua importância ambiental e socioeconômica para o Brasil.* [S.l.]: Instituto de Geociências, Universidade de São Paulo.

Holz, M., França, A. B., Souza, P. A., Iannuzzi, R., & Rohn, R. (2010). A Stratigraphic Chart of the Late Carboniferous/Permian Succession of the Eastern Border of the Paraná Basin, Brazil, South America. *Journal of South American Earth Sciences, 29,* 381-399. https://doi.org/10.1016/j.jsames.2009.04.004

Kronbauer, D. P. (2014). *Determinação de Propriedades Petrofísicas de Rochas Reservatórios usando Modelos de Redes de Poros.* Tese de doutorado, Universidade Federal de Santa Catarina.

Lavina, E. L. (1991). *Geologia sedimentar e paleogeografia do Neopermiano e Eotriássico (Intervalo Kazaniano-Citiano) da Bacia do Paraná* (332 p). Tese de Doutora-mento, Instituto de Geociências, Universidade Federal do Rio Grande do Sul.

Lucas, S. G., & Shen, S. (2018). The Permian Timescale: An Introduction. *Geological Society, London, Special Publications, 450,* 1-19. https://doi.org/10.1144/sp450.15

Maithel, S. A., Brand, L. R., & Whitmore, J. H. (2021). Characterization of Hard-to-Differentiate Dune Stratification Types in the Permian Coconino Sandstone (Arizona, USA). *Sedimentology, 68,* 238-265. https://doi.org/10.1111/sed.12774

Manna, M. O. (2024). *Arquitetura deposicional e padrões de preenchimento de ba-cias endorreicas: Estudo de caso da formação rio do rasto, bacia do paraná, brasil, e da formação yaguarí, bacia do norte, uruguai.* Tese (Doutorado), Universidade Federal do Rio Grande do Sul.

Milani, E., Rangel, H., Bueno, G., Stica, J., Winter, W., Caixeta, J., & Neto, O. (2007). Bacias Sedimentares Brasileiras-Cartas Estratigraficas. *Boletim de Geociências da Petrobras, 15,* 183-205.

Monsees, A. C., Busch, B., & Hilgers, C. (2021). Compaction Control on Diagenesis and Reservoir Quality Development in Red Bed Sandstones: A Case Study of Permian Rotliegend Sandstones. *International Journal of Earth Sciences, 110,* 1683-1711. https://doi.org/10.1007/s00531-021-02036-6

Neto, J. M. R., Fiori, A. P., Lopes, A. P., Marchese, C., Pinto-Coelho, C. V., Vasconcellos, E. M. G. et al. (2011). A microtomografia computadorizada de raios x integrada à petrografia no estudo tridimensional de porosidade em rochas. *Revista Brasileira de Geociências, 41,* 498-508. https://doi.org/10.25249/0375-7536.2011413498508

Ng, C., Vega, C. S., & Maranhão, M. D. S. A. S. (2019). Mixed Carbonate-Siliciclastic Microfacies from Permian Deposits of Western Gondwana: Evidence of Gradual Marine to Continental Transition or Episodes of Marine Transgression? *Sedimentary Geology, 390,* 62-82. https://doi.org/10.1016/j.sedgeo.2019.07.006

Parnell, J. (1987) Secondary Poroslty in Hydrocarbon-Bearing Transgressive Sandstones on an Unstable Lower Palaeozoic Continental Shell, Welsh Borderland. *Geological Society, London, Special Publications, 36,* 297-312. https://doi.org/10.1144/GSL.SP.1987.036.01.21

Porto, A. L. (2015). *Estimação de propriedades petrofísicas de rochas sedimentares a partir de imagens microtomográficas de raíos-x.* Doutorado em Engenharia de Processo, Centro de Ciências e Tecnologia, Universidade Federal de Campina Grande.

Rohn, R. (1994). *Evolução ambiental da Bacia do Paraná durante o neopermiano no leste de Santa Catarina e do Paraná.* Tese de doutorado. Universidade de São Paulo. Instituto de geociências.

Schemiko, D. C. B., Vesely, F. F., Fernandes, L. A., & Sowek, G. A. (2014). Distinção dos elementos deposicionais fluviais, eólicos e lacustres do membro morro pelado, permiano superior da bacia do paraná. *Geologia USP. Série Científica, 14,* 29-46. https://doi.org/10.5327/z1519-874x201400030003

Scherer, C. M. S., Reis, A. D., Horn, B. L. D., Bertolini, G., Lavina, E. L. C., Kifumbi, C. et al. (2023). The Stratigraphic Puzzle of the Permo-Mesozoic Southwestern Gondwana: The Paraná Basin Record in Geotectonic and Palaeoclimatic Context. *Earth-Science Reviews, 240,* Article 104397. https://doi.org/10.1016/j.earscirev.2023.104397

Schneider, R. L., Mühlmann, H., Tommasi, E., Medeiros, R. A., Daemon, R. F., & Nogueira, A. A. (1974). Revisão estratigráfica da Bacia do Paraná. *XVIII Congresso Brasileiro de Geologia, 1,* 41-65.

Shanmugam, G. (1985). Types of Porosity in Sandstones and Their Significance in Interpreting Provenance. In G. G. Zuffa (Ed.), *Provenance of Arenites* (pp. 115-137). Springer. https://doi.org/10.1007/978-94-017-2809-6_6

Sonka, M., Hlavac, V., & Boyle, R. (2013). *Image Processing, Analysis, and Machine Vision.* Fourth Edition. Cengage Learning.

Tiab, D., & Donaldson, E. C. (2024). *Petrophisics: Theory and Practice of Measuring Reservoir Rock and Fluid Transport Properties* (5th ed.). Elsevier.

Toledo, J. C. (2023). *Interações flúvio-eólicas no contexto fluvial distributivo da Formação Rio do Rasto (Guadalupiano-Lopingiano), Bacia do Paraná.* Dissertação (Mestrado), Universidade Federal do Rio Grande do Sul.

Warren, L. V., Almeida, R. P. D.; Hachiro, J., Machado, R., Roldan, L. F., Steiner, S. dos S., & Chamani, M. A. C. (2008). Evolução sedimentar da Formação Rio do Rasto (Permo-Triássico da Bacia do Paraná) na porção centro sul do estado de Santa Catarina, Brasil. *Revista Brasileira de Geociências, 38,* 1-15.

Zalán, P. V., Wolff, S., Astolfi, M. A. M., Vieira, I. S., Concelção, J. C. J., Appi, V. T. et al. (1990). The Paraná Basin, Brazil. In M. W. Leighton, D. R. Kolata, D. F. Oltz, & J. J. Eidel (Eds.), *Interior Cratonic Basins* (pp. 681-708). American Association of Petroleum Geologists. https://doi.org/10.1306/m51530c34